The Mesoscale Dynamics of Thin Tropical Tropopause Cirrus

DALE R. DURRAN AND TRA DINH

Department of Atmospheric Sciences, University of Washington, Seattle, Washington

MARIE AMMERMAN

Iberdrola Renewables, Portland, Oregon

THOMAS ACKERMAN

Department of Atmospheric Sciences, University of Washington, Seattle, Washington

(Manuscript received 22 December 2008, in final form 20 March 2009)

ABSTRACT

Thin cirrus clouds in the tropical tropopause layer (TTL) are warmed through the absorption of infrared radiation. The response of the cloud and the surrounding atmosphere to this thermal forcing is investigated through linear theory and nonlinear numerical simulation. Linear solutions for the circulations forced by a fixed heat source representative of TTL cirrus clouds show ascent in the region of the heating, accompanied by horizontal flow toward the heat source at the base of the heated layer and horizontal outflow at the top of the layer. Gravity waves propagate positive temperature perturbations well beyond the lateral edges of the heated region. Cool layers that also spread horizontally are produced immediately above and below the heated region.

Numerical simulations with a cloud-resolving model allow the radiative heating to change in response to the redistribution of the cloud by the evolving velocity field. The basic atmospheric response in the numerical simulations is nevertheless similar to that generated by the fixed heat source. In the numerical simulations, the advection of ice crystals by the radiatively forced velocity field also lofts the cloud, while horizontally spreading its top and narrowing its base. Ice crystal sedimentation is neglected in these calculations, but it appears that the radiatively induced upward vertical velocities are likely strong enough to maintain clouds consisting of very small crystals (radii less than 4 μm) against sedimentation for many hours.

1. Introduction

Cirrus is ubiquitous in the tropical atmosphere, particularly in convective regions. Pfister et al. (2001) used lidar data from the National Aeronautics and Space Administration (NASA) DC-8 and back-trajectory analyses to argue that tropical cirrus came from two different sources, large-scale uplift and deep convection, and had different textural properties depending on the source. Comstock et al. (2002) used lidar and millimeter-wavelength radar observations to compile a climatology of cirrus clouds over Nauru in the equatorial Pacific. They found that cirrus over Nauru divide into two categories based on altitude. The higher-altitude cirrus, above 15 km, were in the tropical tropopause layer (TTL) and relatively featureless compared to the cirrus detected at lower levels of 8 to 15 km.

Although its exact frequency of occurrence has been difficult to determine, several observational studies (Wang et al. 1996; Peter et al. 2003; Dessler et al. 2006; Liu 2007) have established that thin TTL-level cirrus is common in the tropics. Mace et al. (2009), for example, recently analyzed satellite-based Cloud–Aerosol Lidar and Infrared Pathfinder Satellite Observations (CALIPSO) lidar data from December 2006 through June 2007 and found that cirrus with cloud bases above 14 km occurred between 20% and 30% of the time over many regions in tropics. TTL cirrus were found to occur most frequently just east of the date line, which was also east of the region of most frequent deep convection and thicker upper-tropospheric cirrus.

Corresponding author address: Dale R. Durran, Department of Atmospheric Sciences, University of Washington, Box 351640, Seattle, WA 98195.
E-mail: durrand@atmos.washington.edu

DOI: 10.1175/2009JAS3046.1

The radiative heating of thin TTL cirrus has been estimated as sufficient to produce temperature increases of at least 2–3 K day^{-1} (Jensen et al. 1996b; McFarquhar et al. 2000; Comstock et al. 2002) and could potentially exert a significant influence on the radiative balance of the TTL. This heating has been widely appreciated as having the potential either to warm and dissipate the cloud or to induce upward motion (Jensen et al. 1996b). If the heating does induce a persistent ascent of the cirrus layer, these clouds may play an important role in the transport of water vapor into the tropical stratosphere (Jensen et al. 1996a; Corti et al. 2006). The possible responses of thin TTL cirrus to radiative heating and the possible role of cirrus in stratospheric dehydration are similar to that first proposed for thicker cirrus directly generated in thunderstorm anvils (Danielsen 1982; Ackerman et al. 1988; Lilly 1988).

Despite its importance, few previous studies have focused on determining the dynamical response of thin TTL cirrus to radiative heating. Perhaps the most thorough investigation of the mesoscale dynamics of these clouds was conducted by Boehm et al. (1999), who simulated the evolution of a cirrus layer using a two-dimensional mesoscale cloud model. They found the cloud dissipated within several hours because of the radiative heating, but by choosing an initial cloud that spanned the full horizontally periodic domain, they eliminated possible cloud-scale circulations in which ascent in the cloudy region is balanced by descent in the surrounding clear air. A different approach was pursed by Lilly (1988), who described the mesoscale lifting of a cirrus anvil outflow plume using an analogy to stratified flow around a rising plate. His characterization of the resulting flow is similar in many ways to that obtained via more rigorous analysis in this paper—although, as will be described later, Lilly did not anticipate the extent to which thermally generated gravity waves propagate the disturbance laterally away from the cloud.

In the following we examine the cloud-scale circulations that develop in response to the radiative heating of thin cirrus. We begin, in section 2, by considering linear analytic solutions describing the two-dimensional response of a stratified atmosphere to a fixed heat source similar in shape to a layer of thin TTL cirrus. These solutions are then compared to numerical solutions from a mesoscale cloud model in section 3. Section 4 contains the conclusions.

2. Gravity waves forced by a fixed heat source

The response of a stably stratified Boussinesq fluid to local heating has been previously studied in various contexts (Lin and Smith 1986; Nicholls et al. 1991; Pandya et al. 1993). Here we modify the solution in Pandya et al. (1993) to obtain expressions for the two-dimensional response to localized heating in an unbounded x–z plane. Coriolis forces are neglected both to allow the computation of an analytic solution and because our focus is on motions in the deep tropics.

This two-dimensional framework is rigorously justified when the variations in all fields along the y coordinate are negligible, which is probably not the case for actual TTL cirrus. In comparison to the two-dimensional problem, the three-dimensional disturbance generated by IR heating in a roughly circular cloud will be qualitatively similar near the cloud itself but will decay more rapidly away from the cloud edge and be much weaker at very large distances from that center. Nevertheless, we employ the two-dimensional framework to obtain a concise analytic solution to the linearized problem and to economically perform very high-resolution numerical simulations.

a. Analytic solutions for the vertical velocity

The governing equations for quasi-hydrostatic flow, linearized about a resting basic state in a two-dimensional Boussinesq fluid, may be expressed as

$$\frac{\partial u}{\partial t} + \frac{\partial P}{\partial x} = 0, \tag{1}$$

$$\frac{\partial P}{\partial z} - b = 0, \tag{2}$$

$$\frac{\partial u}{\partial x} + \frac{\partial w}{\partial z} = 0, \tag{3}$$

$$\frac{\partial b}{\partial t} + N^2 w = Q, \tag{4}$$

where u is horizontal velocity, w is vertical velocity, P is the Boussinesq pressure potential, and b is the buoyancy. In an atmospheric context, it is most appropriate to define P and b in terms of the Exner function pressure $\Pi = (p/p_0)^{R/c_p}$ and potential temperature $\theta = T/\Pi$, where p is pressure, p_0 is a constant reference pressure, and T is the sensible temperature. Then

$$P = c_p\theta_0(\Pi - \overline{\Pi}) \quad \text{and} \quad b = \frac{g(\theta - \overline{\theta})}{\theta_0},$$

where overbars denote vertically varying basic-state thermodynamic fields in hydrostatic balance and θ_0 is a constant reference value. In addition, $N^2 = (g/\theta_0)(d\overline{\theta}/dz)$ is the square of the Brunt–Väisälä frequency, $Q = (g\dot{H})/(c_pT_0)$ is the thermal forcing for buoyancy, $\dot{H}$ is the rate of diabatic heating per unit mass, and T_0 is a reference temperature characteristic of the TTL.

Note that if the system (1)–(4) is nondimensionalized using the scales $u = \alpha\mathcal{U}\hat{u}$, $b = \alpha\mathcal{B}\hat{b}$, $P = \alpha\mathcal{P}\hat{P}$, $t = \alpha\mathcal{T}\hat{t}$, $x = \alpha\mathcal{X}\hat{x}$, $w = \mathcal{W}\hat{w}$, and $z = \mathcal{Z}\hat{z}$, the result is independent of the constant α. Thus, if the vertical coordinate is fixed while the horizontal and time coordinates are stretched by the factor α, any solution in the original coordinates may be mapped to a solution in the stretched coordinates by increasing the magnitude of the u, b, and P fields by a factor of α, while leaving the amplitude of the w field unchanged.[1]

A heat source roughly representative of that which might be produced in a cirrus cloud that is optically thin in the IR is specified as

$$Q(x, z) = Q_0 \frac{a^2}{x^2 + a^2} \begin{cases} \cos\left(\dfrac{\pi z}{2H}\right) & \text{if} \quad |z| < H, \\ 0 & \text{otherwise.} \end{cases} \tag{5}$$

Here, $2H$ is the depth of the heating and a is the half-width at half amplitude. In the following we set $H = 250$ m and take a as either 20 or 100 km; these choices yield a 500-m-thick cloud whose total width is roughly 100 or 500 km. The buoyancy forcing in the center of the cloud is $Q_0 = 1.75 \times 10^{-6}$ m s^{-3}; choosing $T_0 = 193$ K, this value of Q_0 corresponds to a sensible heating rate $\dot{H}/c_p$ of 3.0 K day^{-1}, which approximates the 3.1 K day^{-1} heating estimated for TTL cirrus by Comstock et al. (2002) and matches the 3.0 K day^{-1} recently determined from data collected on a flight through TTL cirrus off the east coast of Nicaragua by A. Bucholtz et al. (2009, unpublished manuscript, hereafter BHM). The heating is symmetric about $x = 0$; the distribution of $\dot{H}/c_p$ in the right half-plane is shown in Fig. 1. There are no initial perturbations and the heating is turned on instantaneously at $t = 0$.

Pandya et al. (1993) considered a situation relevant to deep convection in which a relatively deep and narrow region of heating is adjacent to a rigid lower boundary. Using our notation, their solution satisfies $w(x, -H, t) = 0$. When modeling TTL cirrus, it is more appropriate to simply neglect the effects of the earth's surface and compute the circulation in an unbounded vertical plane. Modifying the approach described in Pandya et al. (1993) to account for this different lower boundary condition, the vertical velocity forced by (5) becomes

$$w(x, z, t) = \frac{Q_0 m a}{N^3 t} \mathrm{Re}\left[\frac{\lambda^2}{1 + \lambda^2}(e^{-\lambda\mu_>} \cosh\lambda\mu_< + \lambda \cos\mu_<)\right], \tag{6}$$

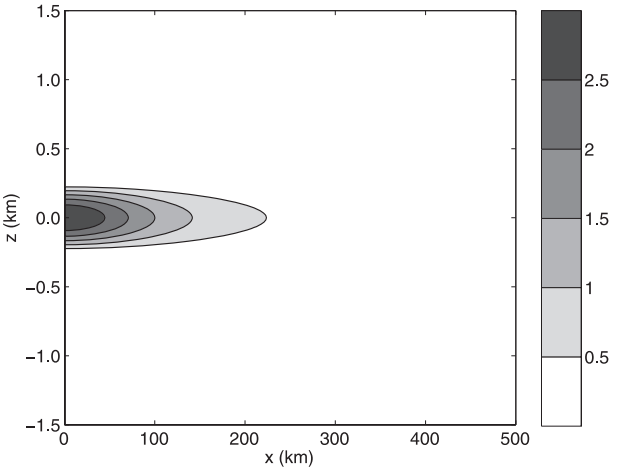

FIG. 1. Sensible heating rate QT_0/g for the case $a = 100$ km, contoured at an interval of 0.5 K day^{-1}.

where

$$\lambda = \frac{\gamma N t}{m}, \quad \mu_> = m \max(|z|, H), \quad \mu_< = m \min(|z|, H), \tag{7}$$

in which

$$m = \frac{\pi}{2H}, \quad \gamma = \frac{a + ix}{a^2 + x^2}.$$

Analytic solutions for u and b are not available; values are obtained numerically by substituting the solution for w into (3) or (4), respectively.

b. The evolving perturbation fields

The circulations that develop in response to this heat source are shown in Fig. 2 for the case $a = 100$ km, $N = 0.016$ s^{-1} at times $t = 15$ and 30 h. There is horizontal inflow toward the origin for $z < 0$, upward motion inside the heating region, and horizontal flow away from the origin for $z > 0$. The perturbations, including potential temperature perturbations $\theta' = \theta - \overline{\theta}(z)$, are seen to spread laterally away from the region of heating. Note in particular that *warming occurs over a much wider region than the width of the heat source itself.* Provided that the amplitude is sufficiently small, the disturbances forced by heating in a stratified fluid are linear gravity waves. The angle ϕ between the vertical coordinate and the rays along which gravity waves propagate is given by $\omega = N\cos\phi$, where ω is the wave's frequency. For $t > 0$, the frequency of the thermal forcing is steady and will therefore tend to force disturbances for which $\phi = 90°$. Thus, except at the leading edge of the disturbance, where the influence of the initial

[1] This result also generalizes to the 3D case, but not when Coriolis forces are included.

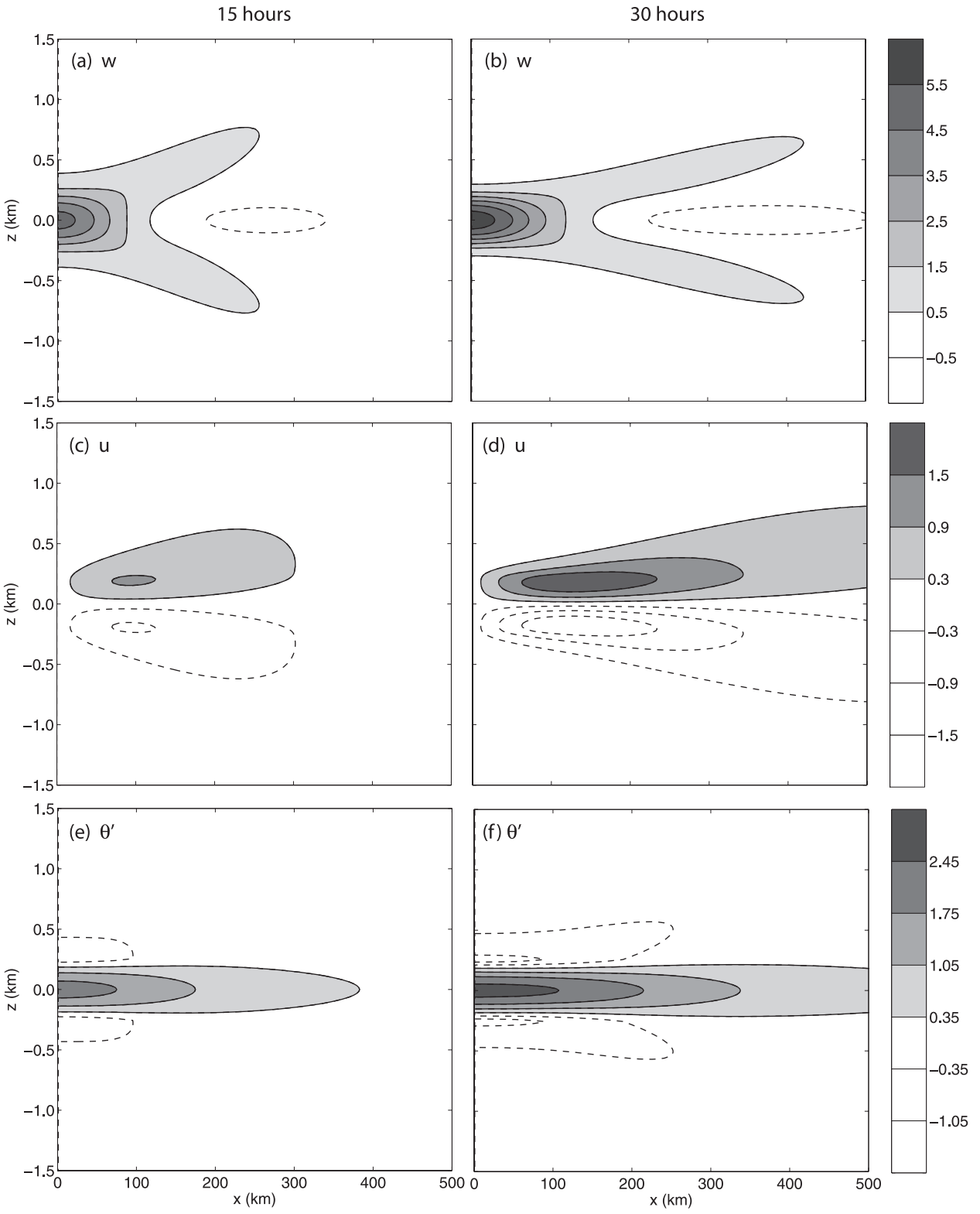

FIG. 2. Gravity wave response for the case $a = 100$ km at $t =$ (left) 15 and (right) 30 h. Contoured fields are (a),(b) w in mm s^{-1}, (c),(d) u in m s^{-1}, and (e),(f) perturbation potential temperature in K. Positive values are shaded and contoured by solid lines; negative values are contoured by dashed lines.

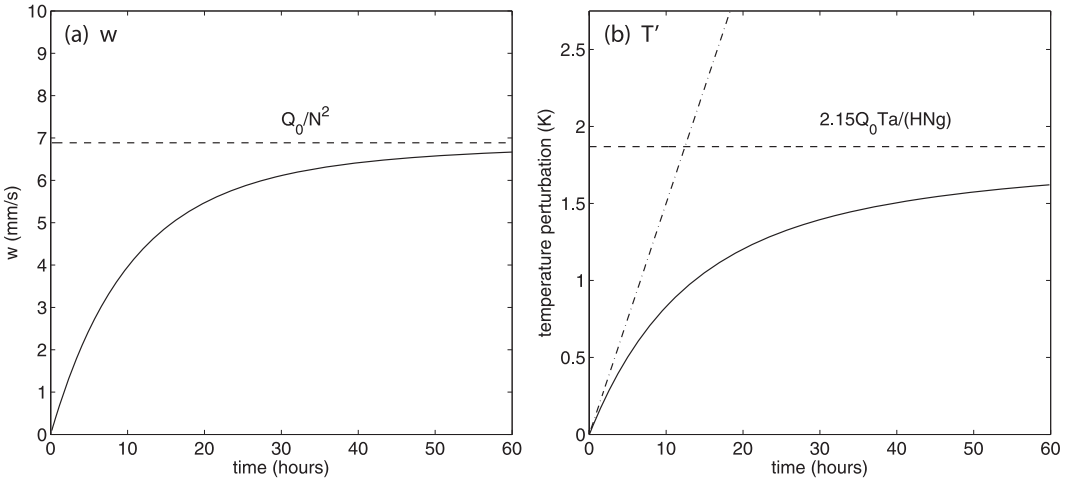

FIG. 3. Solid lines show the approach to steady state of (a) vertical velocity w (mm s^{-1}) and (b) sensible temperature perturbation T' (K) as a function of time. Dashed lines are the steady-state solutions. The dashed–dotted line in (b) shows the temperature perturbation that would result from a local temperature increase of 3.0 K day^{-1}.

transients is most pronounced, the signal propagates almost horizontally away from the region of heating.

The propagation of the disturbance results not from advection but rather from gravity wave dynamics. The positive potential temperature perturbation expands laterally beyond the region of significant diabatic heating due to adiabatic warming forced by subsidence, such as that at $x = 300$ km in Fig. 2a. Negative temperature perturbations, which also expand horizontally, are similarly generated by adiabatic cooling above and below the heat source. The gravity wave phase speed for linear waves is independent of the wave amplitude (and the strength of the velocity perturbations). The gravity wave phase speed for hydrostatic waves of half-wavelength equal to the $2H$ depth of the heated region is $2NH/\pi$, which is 2.5 m s^{-1} for the case shown in Fig. 2.[2]

Lilly (1988) used stratified flow around a rising flat plate as a heuristic model for the mesoscale lifting of a cirrus cloud. Many of the features of his schematic Fig. 8 are qualitatively captured by the solutions shown in Fig. 2, including layers of horizontal inflow and outflow at the bottom and top of the cloud and layers of adiabatically cooled air just above and below the cloud. Lilly did not, however, correctly depict the positive temperature perturbations in the cirrus layer or their lateral propagation well away from the cloud edge, and he also did not anticipate that most of the horizontal inflow and outflow is vertically confined to the layer containing the cloud itself.

At any given point in the domain, the perturbations gradually approach a steady state. The steady-state vertical velocity field, which can be obtained either from (4) or as the $t \to \infty$ limit of (6), is

$$w_{ss}(x, z) = \frac{Q(x, z)}{N^2} = \frac{Q_0}{N^2}\frac{a^2}{x^2 + a^2}\begin{cases}\cos\left(\dfrac{\pi z}{2H}\right) & \text{if} \quad |z| < H, \\ 0 & \text{otherwise.}\end{cases} \tag{8}$$

Using the preceding and the incompressible mass continuity Eq. (3), one can show that

$$u_{ss}(x, z) = \frac{Q_0}{N^2}\frac{\pi a}{2H}\begin{cases}\arctan\left(\dfrac{x}{a}\right)\sin(mz) & \text{if} \quad |z| < H, \\ 0 & \text{otherwise.}\end{cases} \tag{9}$$

The steady-state vertical velocity field has the same shape as the heating, and its amplitude only depends on the magnitude of the heating and the Brunt–Väisälä frequency. The magnitude of the steady-state horizontal velocity has the same dependence on Q_0/N^2 but is also inversely proportional to its depth $2H$. In addition, at equivalent nondimensional horizontal distances x/a, u_{ss} is proportional to the width of the cloud.

Figure 3 shows how $w(0, 0, t)$ and $T(0, 0, t)$ approach steady state for the case shown in Fig. 2. From (6), the vertical velocity at the origin is

$$w(0, 0, t) = \frac{Q_0}{N^2}\frac{\lambda}{1 + \lambda^2}\left(e^{-\pi\lambda/2} + \lambda\right). \tag{10}$$

[2] The −0.35- and 1.75-K contours propagate at about this speed (cf. Figs. 2e,f), although other contour lines in Fig. 2 translate at a range of different speeds because the vertical structure of the disturbance is not a single monochromatic wave and because the disturbance is intensifying as well as simply propagating.

As illustrated in Fig. 3a, the time required to approach steady state is roughly 2 days. In reality, TTL cirrus form gradually on a finite time scale and may never be subject to transients as large as those in our initial value problem. Nevertheless for very wide clouds (on the order of 500 km, which corresponds to the choice $a = 100$ km), the steady-state approximation $w = Q/N$ (Corti et al. 2006) may not be accurate over a significant fraction of the cloud's lifetime.

The steady-state temperature perturbation at the origin $T'_{ss}(0, 0)$ can be computed from the buoyancy perturbation by integrating Eq. (4),

$$b_{ss}(x, z) = \int_0^\infty (Q - N^2 w)\, dt, \tag{11}$$

and using (10) to produce

$$b_{ss}(0, 0) = \frac{Q_0 am}{N} \int_0^\infty \frac{1}{1+\lambda^2}\left(1 - \lambda e^{-\pi\lambda/2}\right) d\lambda \approx 2.15 \frac{Q_0 a}{NH}. \tag{12}$$

Because the pressure perturbations are very small compared to the mean hydrostatic pressure, $T' = \overline{\Pi}\theta' = (\overline{\Pi}\theta_0 b)/g \equiv T_0 b/g$, which using (12) yields a value of $T'_{ss}(0, 0) = 1.85$ K (indicated by the horizontal dashed line in Fig. 3b). As shown in Fig. 3b, the temperature perturbation approaches steady state more slowly than the velocity perturbation. It is also apparent in Fig. 3b that after roughly 5 h the rate of increase in temperature at the center of the heating region begins to deviate significantly from that which would be realized if all heating contributed to a local rise in temperature, the difference between the solid curve and dotted–dashed line in Fig. 3b being due to heat transport by gravity waves. For example, 60 h of heating at a rate of 3.6 K day^{-1} would, absent other factors, lead to a local temperature increase of 9 K, whereas the actual temperature increase over the same period is just under 2 K.

Lilly (1988) arrived at an expression for the steady-state temperature perturbation [his Eq. (4.6)] having the same functional dependence on the environmental parameters Q_0, a, N, and H as that in (12), although he estimated that a heating rate of about 21 K day^{-1} would produce only a 0.3 K steady-state temperature perturbation.[3] Compared to our results, Lilly obtains a much weaker response from much stronger thermal forcing, primarily because his 25-km-wide cloud is much smaller than the 500-km-wide specimen considered in our example. In addition, his cloud is thicker and is embedded in a layer of weaker static stability. Finally, Lilly took the constant of proportionality c as unity in his Eq. (4.6), whereas the equivalent quantity evaluated from (12) is roughly 3.

Let t_s be the time scale required for the vertical velocity to approach steady state at some fixed point within the heating layer, (x, z) where $|z| \le H$; this time scale can be estimated as follows: Suppose ϵ is a small parameter ($\epsilon \ll 1$) such that

$$w(x, z, t_s) = (1 - \epsilon) w_{ss}(x, z). \tag{13}$$

The simplest expression for t_s is obtained at the origin. From (8), (10), and (13) we have

$$w(0, 0, t_s) = \frac{Q_0}{N^2} \frac{\lambda_s}{1+\lambda_s^2}\left(e^{-\pi\lambda_s/2} + \lambda_s\right) = (1 - \epsilon)\frac{Q_0}{N^2}, \tag{14}$$

where $\lambda_s = Nt_s/ma$. [Recall that λ was given by (7).] Assuming t_s is sufficiently large that we can neglect $e^{-\pi\lambda_s/2}$ compared with λ_s, then (14) implies $\lambda_s \approx \epsilon^{-1/2}$, or

$$t_s \approx \frac{am}{N\epsilon^{1/2}} = \frac{a\pi}{2HN\epsilon^{1/2}}. \tag{15}$$

This result is consistent with the assumption that $e^{-\pi\lambda_s/2}$ can be neglected when ϵ is sufficiently small.

Using similar reasoning and noting that for t_s sufficiently large

$$\frac{\lambda_s^3}{1+\lambda_s^2} = \frac{\lambda_s}{1/\lambda_s^2 + 1} \approx \lambda_s - \frac{1}{\lambda_s},$$

one may show that the time scale required to approach steady state elsewhere in the heating layer ($|z| < H$) is

$$t_s(x, z) \approx \frac{m(a^2 + x^2)^{1/2}}{N\epsilon^{1/2}} = \frac{\pi(a^2 + x^2)^{1/2}}{2HN\epsilon^{1/2}}. \tag{16}$$

Thus, it takes longer to approach steady state if the heat source is wider or shallower, or if the atmosphere is less stable. According to (16), the farther the horizontal distance to the center of the heat source (the larger $|x|$ is), the longer it takes to reach steady state. Out toward the edge of the cloud at $x = 2a$, the time scale to approach steady state is a factor of $\sqrt{5}$ longer than at the origin.

[3] Lilly gives values for *potential* temperature perturbations and heating rates, which at the pressure altitude of TTL cirrus are roughly twice the values for sensible temperature given here.

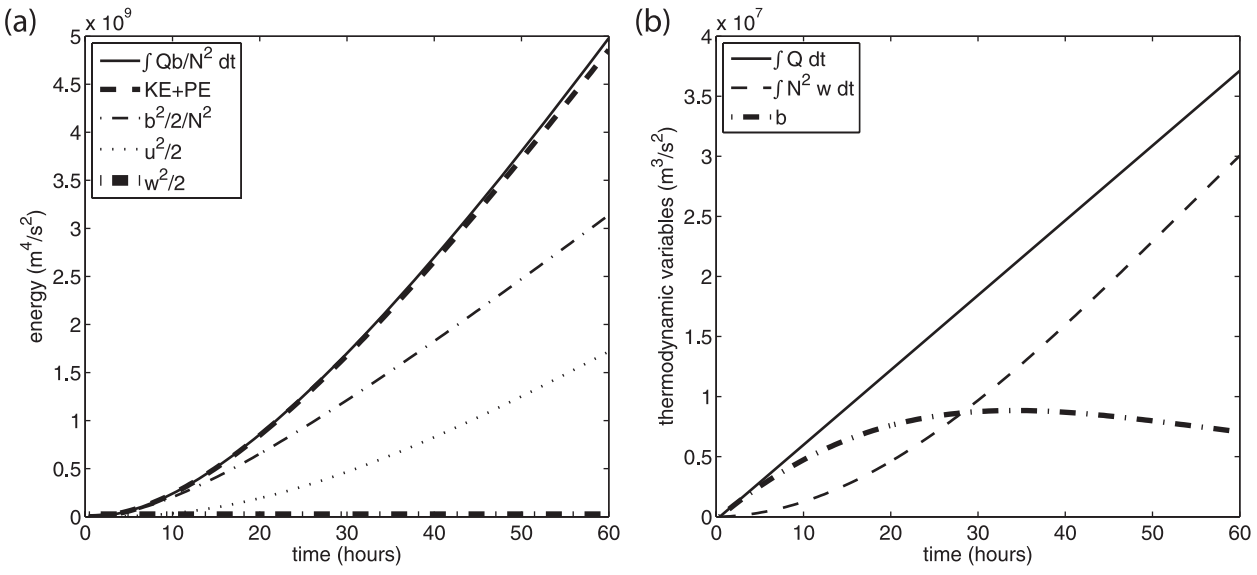

FIG. 4. Terms making up the domain-integrated (a) energy budget and (b) thermodynamic budget plotted as a function of time for the case $a = 100$ km.

c. *The domain-integrated energy budget*

The total energy budget (per unit mass) for the perturbation fields satisfies

$$\frac{\partial}{\partial t}\left(\frac{u^2}{2}+\frac{w^2}{2}+\frac{b^2}{2N^2}\right)+\frac{\partial}{\partial x}(Pu)+\frac{\partial}{\partial z}(Pw)=\frac{Qb}{N^2}. \tag{17}$$

The first two terms in the time derivative are the perturbation kinetic energy (KE); the last term is the perturbation potential energy (PE) (Gill 1982, p. 139). If (17) is integrated over a sufficiently large domain at any finite time, the divergence of the energy flux $\partial_x u + \partial_z w$ is zero because the disturbance has not yet reached the boundary. The integral of the terms in (17) over such a domain, which will be denoted by $\langle\ \rangle$, is shown as a function of time in Fig. 4a. The slight difference between the curves for the time-integrated domain-averaged energy input and for $\langle \mathrm{KE}\rangle + \langle \mathrm{PE}\rangle$ is due to the placement of the boundaries of the domain for the budget computations at a finite distance from the heat source. (The integrals in Fig. 4 are computed over the domain $-2000 \le x \le 2000$ km, $-2 \le z \le 2$ km.) The largest response to the heating appears in $\langle \mathrm{PE}\rangle$; $\langle \mathrm{KE}\rangle$ is roughly half the size of $\langle \mathrm{PE}\rangle$ and, consistent with the very hydrostatic nature of the response, is dominated by contributions from the horizontal velocity field.

The domain-integrated buoyancy field, along with the other terms in (4) that make up the thermodynamic energy budget, is plotted in Fig. 4b. Although potential energy perturbations dominate the total energy budget, as apparent in Fig. 4b, after about hour 20 most of the heating produces vertical motions rather than additional increases in $\langle b\rangle$. Indeed, after hour 30, $\langle b\rangle$ starts to decline.[4] It may appear odd that the potential energy associated with buoyancy accounts for the largest fraction of the energy input (Fig. 4a) whereas $\langle b\rangle$ accounts for only a small fraction of the total heating. The domain-integrated buoyancy $\langle b\rangle$ remains much smaller than $\langle b^2\rangle$ because after the initial transient, negative buoyancy perturbations develop above and below the heated layer (Figs. 2e,f). These expanding regions of negative buoyancy largely offset any tendency for the expanding region of positive buoyancy within the heated layer to increase $\langle b\rangle$.

3. Numerical simulations of radiatively heated TTL cirrus

The linear model presented in the preceding section does not account for the changes in the shape of the cloud that would be produced as ice crystals are transported by the velocity fields induced by the radiative heating. To capture the feedback of the cloud-induced circulation on the geometry of the cloud, we turn to a numerical model. The numerical model used in this study solves the nonhydrostatic governing equations in a two-dimensional x–z plane.

[4] In the particular domain we use to compute $\langle b\rangle$, it eventually approaches a steady-state value of about 0.6×10^7 m^3 s^{-2}.

We focus on thin TTL cirrus, which, being detectable by lidar but not mm radar, likely consist of very small crystals (Comstock et al. 2002). The smallness of the crystals led us to simplify the model by assuming cloud ice has zero fall speed relative to the surrounding air. Having neglected sedimentation, we also neglect other cloud microphysical processes such as changes in crystal radius due to deposition or sublimation, which in turn eliminates the sensitivity of our results to the environmental humidity. (We are in the process of removing these limiting approximations by extending the model to include a bin microphysical scheme with sedimentation and explicit coupling between each ice crystal's size and its radiative properties.)

The model's numerical formulation is similar to the two-time-step compressible formulation presented in Durran and Klemp (1983) except that an almost-monotonicity-reserving positive definite advection scheme (Blossey and Durran 2008) is used for the advection of the potential temperature and moisture variables (which in the present case reduce to just cloud ice). The other significant addition to the model is the radiation scheme, which is described below.

a. Evaluating the radiative forcing

We do not include motions due to large-scale tropical waves or to the mean atmospheric circulation in our simulations. Consistent with our neglect of the large-scale radiatively driven mean descent in the upper troposphere and mean ascent in the lower stratosphere, we also neglect the background radiative heating due to atmospheric gases like water vapor, carbon dioxide, and ozone. Our focus is solely on the absorption of radiation by ice crystals.

Because TTL cirrus are optically thin in both the solar and the infrared, multiple scattering has a minimal effect on the net radiative absorption in the cloud layer and will be neglected. Given that scattering is ignored, the monochromatic transmittance in a plane-parallel atmosphere can be approximated by

$$t_\lambda \approx e^{-\tau_\lambda/\overline{\mu}}, \tag{18}$$

where τ_λ is the optical depth of the layer at wavelength λ and $\overline{\mu}$ is the cosine of the effective zenith angle. Here we will use $\overline{\mu} = \frac{1}{2}$. In the case of TTL cirrus the absorption of radiation by the ice particles dominates gaseous absorption, so this problem can be treated as a single absorber case. This condition allows us to approximate the broadband transmittance of the jth layer as

$$t_j \approx e^{-\overline{\tau}_j/\overline{\mu}}, \tag{19}$$

where $\overline{\tau}_j = \overline{\sigma}_a N_j \Delta z$ is the effective broadband optical depth in the jth layer, $\overline{\sigma}_a$ is the effective broadband absorption cross section, N_j is the ice number density in the layer, and Δz is the depth of the layer. The broadband upward and downward fluxes at the top and bottom of the jth layer are calculated according to

$$F_\uparrow^{j+1/2} = F_\uparrow^{j-1/2} t_j + (1 - t_j) B_j, \tag{20}$$

$$F_\downarrow^{j-1/2} = F_\downarrow^{j+1/2} t_j + (1 - t_j) B_j, \tag{21}$$

where $B_j = \sigma T_j^4$ is the broadband flux emitted by a blackbody, $\sigma = 5.67 \times 10^{-8}$ W m^{-2} K^{-4} is the Stefan-Boltzmann constant, and T_j is the temperature of the jth layer in kelvins. The radiative heating rate in each layer of the atmosphere can then be calculated from the broadband fluxes according to

$$\frac{dT_j}{dt} = \frac{F_\uparrow^{j-1/2} j - F_\uparrow^{j+1/2} + F_\downarrow^{j+1/2} - F_\downarrow^{j-1/2}}{\rho c_p \Delta z}. \tag{22}$$

The remaining issue is how to estimate the effective broadband absorption cross section $\overline{\sigma}_a$. The usual way to do that is to perform an integration across all wavelengths. However, a much simpler approach, which we will use here, is to parameterize $\overline{\sigma}_a$ based on a standard radiative transfer model. More specifically, $\overline{\sigma}_a$ is chosen such that the heating rate calculated in (19)–(22) is the same as what would be obtained from a standard radiative transfer model.

We determined the value of $\overline{\sigma}_a$ using the Rapid Calculation of Radiative Heating Rates (RAPRAD) radiative transfer model introduced by Toon et al. (1989). Toon et al. (1989) derived the tridiagonal matrix that results from the two-stream approximation applied to an atmosphere of multiple homogeneous layers. RAPRAD has 16 wavelength intervals for the longwave spectrum (3.3 to 1000 μm) and 32 wavelength intervals for the shortwave spectrum (0.24 to 4.6 μm). RAPRAD absorption cross sections of the shortwave spectrum were updated by Kato et al. (1999) using the k-distribution method. Using this update, the model transmissivity deviates by no more than 1% from that in a line-by-line reference computation across most of the solar spectrum (Kato et al. 1999).

For our simplified radiation code, instead of having 48 absorption cross-section values as in RAPRAD (16 for the longwave spectrum and 32 for the shortwave spectrum), we parameterize only two effective absorption cross sections, one for the longwave spectrum and one for the shortwave spectrum. This means tolerating some

degree of error in the calculation of the radiative heating rate in comparison with RAPRAD over the range of optical depth relevant to TTL cirrus. The parameterization of the absorption cross section is performed at each particular ice particle size; thus, for each particle size there are two parameterized absorption cross sections.

The boundary conditions necessary to solve for the fluxes in the intermediate levels inside the cirrus cloud are the downward flux at the cloud top and the upward flux at the cloud base. These fluxes are calculated using RAPRAD running on the initial atmospheric temperature, water vapor, and ozone profiles. In all of our simulations the cloud top and bottom appear to move vertically by less than 200 m. This is less than the 300-m minimum grid spacing we used for RAPRAD. Furthermore, we found that the perturbations of the basic atmospheric profile by the cloud dynamics are too small to change the downward flux at the cloud top and the upward flux at the cloud base. Therefore, we assume that these boundary fluxes, once calculated by RAPRAD from the initial conditions, are fixed for all time steps in simulating the cirrus cloud.

The heating rate of the cirrus given by our simplified radiation scheme has been tested against RAPRAD. It is found to be accurate within about 5% for cloud ice absorption optical depths between 0.0005 and 0.05. Single-layer TTL cirrus are generally observed to be within this range of optical depth (Comstock et al. 2002; McFarquhar et al. 2000). Given our focus on the radiatively driven cloud dynamics, our approach provides a reasonable trade-off between efficiency and accuracy.

b. Simulation details and initial conditions

The numerical domain is the region $-200 \le x \le 200$ km, $12 \le z \le 18$ km. Wave-permeable boundaries are approximated at all boundaries. The radiation boundary condition for hydrostatic gravity waves (Klemp and Durran 1983; Bougeault 1983) as formulated in Durran (1999) is imposed at the top boundary. At the lower boundary, a wave-absorbing layer combining Rayleigh and viscous damping occupies the layer between 12 and 14.5 km. The normal velocity at the lateral boundaries is computed using one-way wave equations with outward directed gravity wave phase speeds of 5.5 m s^{-1}. The grid spacing is $\Delta x = 250$ m, $\Delta z = 25$ m, except that below the top of the damping layer Δz increases smoothly as z decreases, achieving a maximum value of 100 m at $z = 12$ km.

The initial cloud in both simulations is 100 km wide, 500 m thick, and centered at $(x, z) = (0, 16.25)$ km. The depth of the cloud layer is similar to that of observed TTL cirrus, but its width is somewhat smaller than that typically observed, which can exceed a thousand kilometers (Winker and Trepte 1998). The width chosen for our cloud was limited by computational resources. All cloud ice particles are initialized with a radius 4.2 μm, which is representative of the observed ice crystal sizes in TTL cirrus [see McFarquhar et al. (2000) for observations of TTL cirrus microphysical properties]. For an ice particle of this size, the parameterized absorption cross sections are 3.7×10^{-11} m^2 (longwave) and 4.7×10^{-13} m^2 (shortwave). In both cases the ice concentration in the center of the cloud is 6.5×10^5 ice particles per cubic meter, a value chosen to give a 3.0 K day^{-1} heating rate at the center of our cloud of 4.2-μm-radius crystals. The infrared absorption optical depth of the entire cloud layer is 0.007.

In the first simulation (case 1), the initial shape of the cloud is similar to the shape of the region of fixed heating shown in Fig. 1. The vertical structure is identical to that in (5) except that the origin is shifted to $z = 16.25$ km. The horizontal structure is $\cos^2(\pi x/100)$ for $x \in [-50, 50]$ km, which approximates the horizontal distribution of the heating in (5) when $a = 20$ km. In case 1, the Brunt–Vaïsälä frequency of the resting background state is constant and identical to the $N = 0.016$ s^{-1} value for which analytic solutions were obtained in the previous section. The radiative heating generated by this initial cloud is shown in Fig. 5a; in this and subsequent figures only the central portion of the right half of the domain is shown. The solution is symmetric about $x = 0$.

Whereas the first simulation is designed to allow a close comparison with the analytic solution for the fixed heat source considered in the previous section, the second case explores a situation more closely representative of the TTL. The vertical distribution of the initial cloud is the same as in case 1, but the central 80 km of the cloud is horizontally uniform. Cloud ice concentrations drop to zero in a $\cos^2$ profile beginning 10 km from the cloud edge. The radiative heating produced by the initial cloud in case 2 is shown in Fig. 5b. The atmospheric sounding for this case is representative of the eastern tropical Pacific (Gettelman et al. 2004); within the TTL the Brunt–Vaïsälä frequency increases from a typical tropospheric value of 0.01 s^{-1} to typical stratospheric values in excess of 0.02 s^{-1}. The environmental profiles of θ and N for case 2 are shown in Fig. 6.

c. Numerical results

The velocity and perturbation potential temperature fields in case 1, which is initialized with a cloud whose structure approximates the shape of the heated region in the previous section, are shown at $t = 6$ h in Figs. 7a,c,e. The main features of the thermally forced gravity waves generated by the fixed heat source (5) are clearly present in the numerical solution, including upward vertical

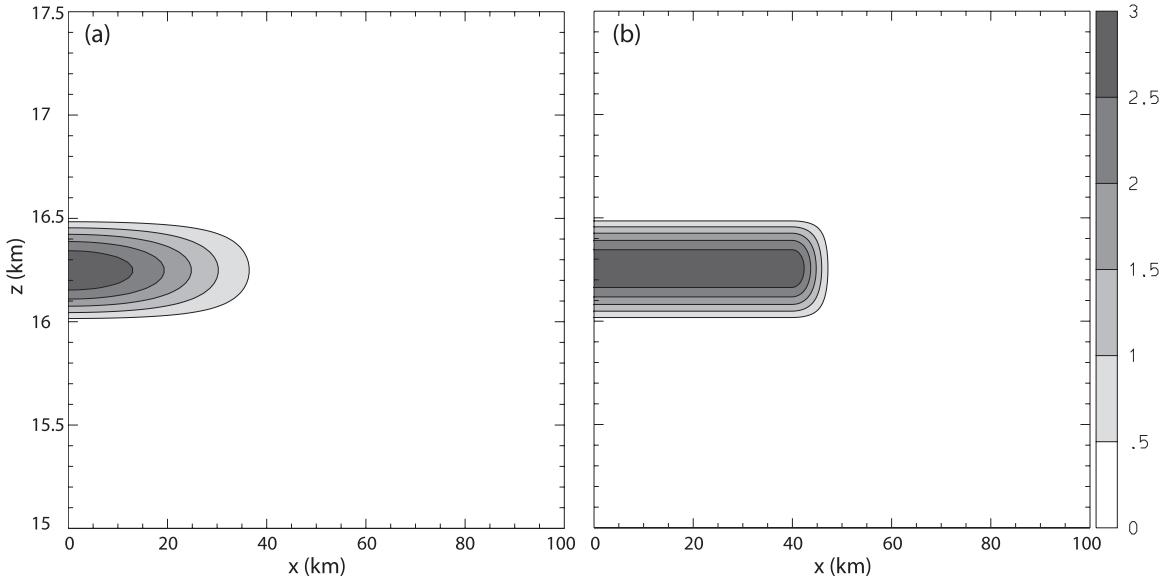

FIG. 5. The initial radiative heating (K day^{-1}) in cases (a) 1 and (b) 2. The heating is symmetric about $x = 0$.

motion inside the cloud and inward/outward horizontal motions in the lower/upper halves of the cloud layer. As before, a horizontal tongue of warm air extends well beyond the region of radiative heating, and adiabatic ascent produces cooling just above and below the heated layer.

Recall that for the analytic solution, x, t, u, and b all scale with the width a of the heating region. Because $a = 100$ km in Fig. 2 but the case shown in Fig. 7 approximates $a = 20$ km, the values of x, u, and b shown at $t = 30$ h in Figs. 2b,d,f should be divided by 5 to compare with those shown at $t = 6$ h in Figs. 7a,c,e. (The z coordinate and the magnitude of the vertical velocity do not change with a.) Allowing for this rescaling, the extrema in the two solutions are very similar. The maximum vertical velocities are almost the same. The horizontal velocities are larger in the numerical simulation, whereas the temperature perturbations are slightly weaker.

One important difference between the case with fixed heating and the problem considered in case 1 is that the numerically simulated cloud rises and its top is stretched relative to its bottom. As a consequence, the fields lose their symmetry about the horizontal centerline of the initial heating at $z = 16.25$ km. The decrease in density with height, which is accounted for in the numerical simulation but neglected in the Boussinesq solution for

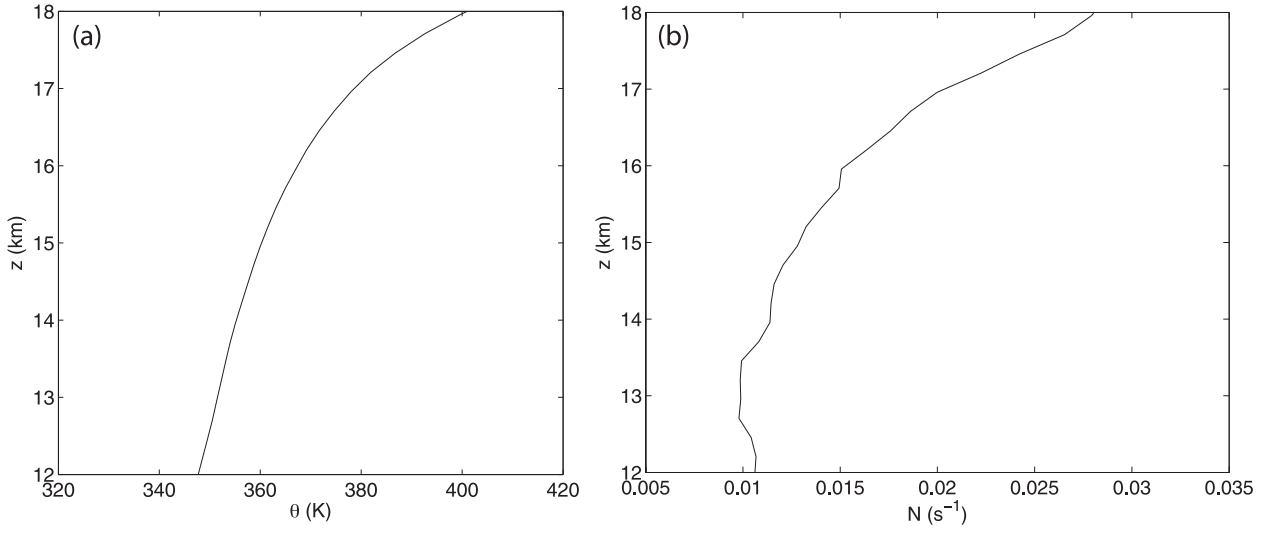

FIG. 6. Vertical profiles of (a) the background potential temperature θ (K) and (b) the Brunt–Vaïsälä frequency N (s^{-1}) for case 2.

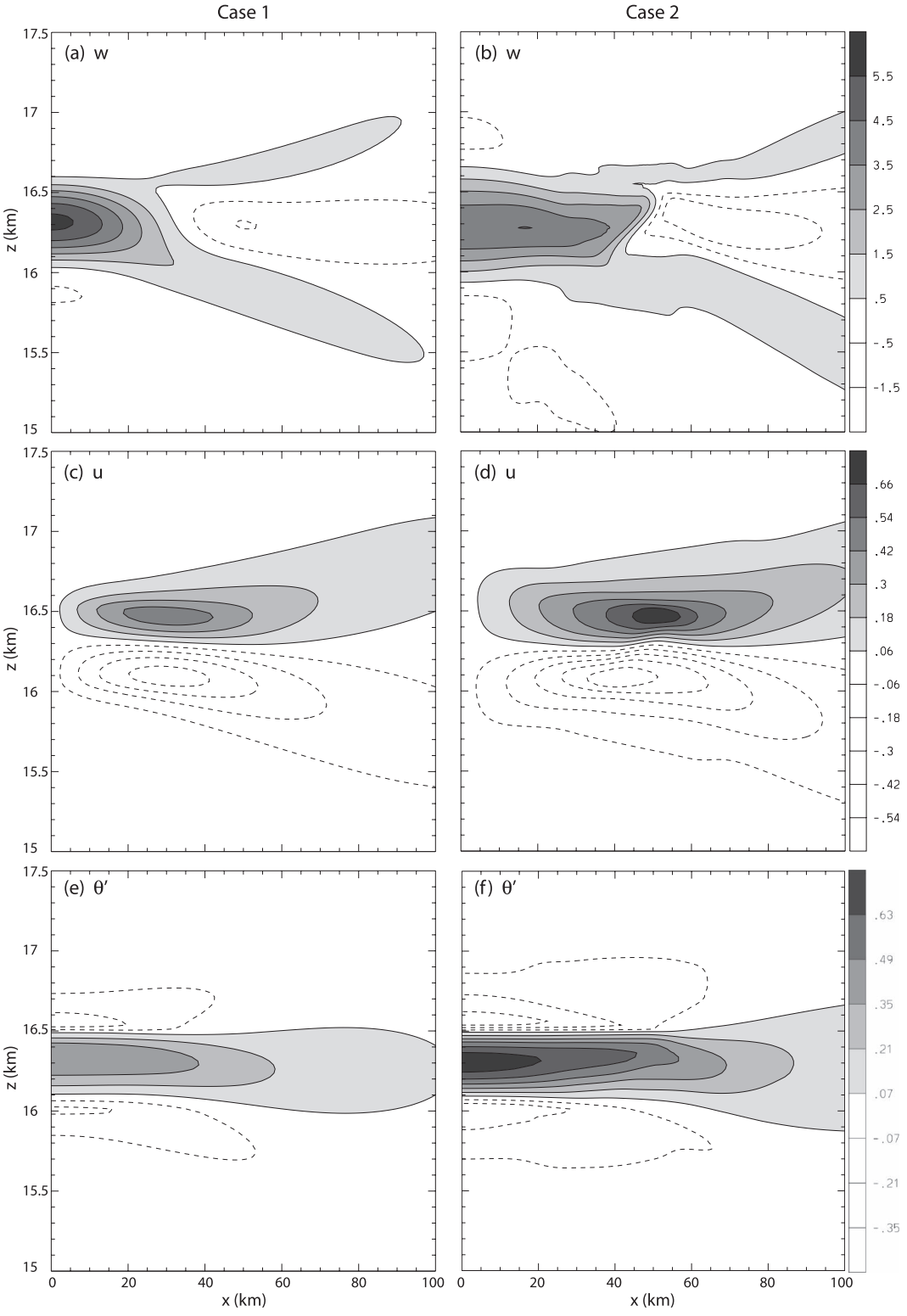

FIG. 7. (a),(b) Vertical velocity (mm s^{-1}), (c),(d) horizontal velocity (m s^{-1}), and (e),(f) perturbation potential temperature (K) for (a),(c),(e) case 1 and (b),(d),(f) case 2. Positive values are contoured by solid lines and highlighted by grayscale fill; negative values are contoured by dashed lines.

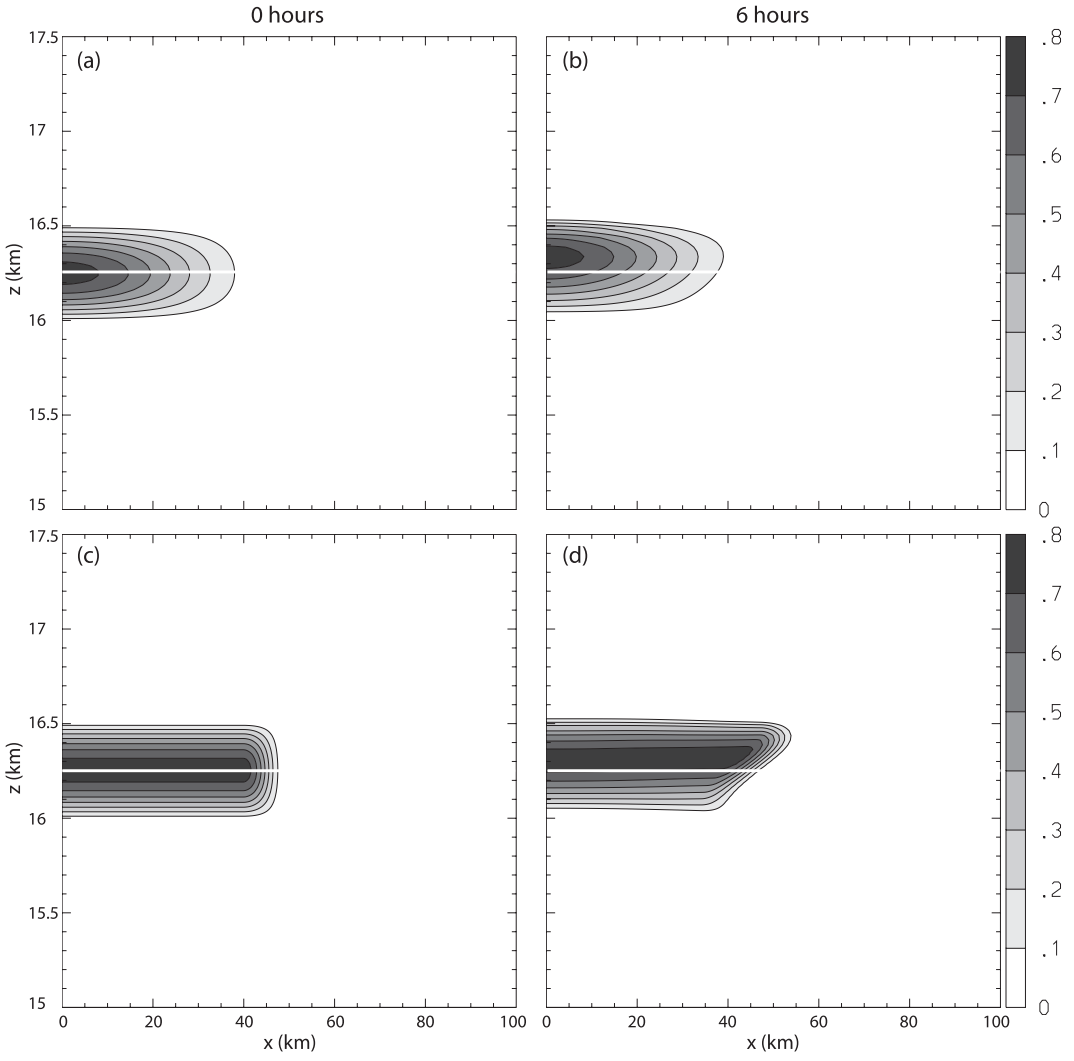

FIG. 8. Ice mixing ratio (in units of 10^{-6} kg kg^{-1}) for t = (a),(c) 0 and (b),(d) 6 h for (a),(b) case 1 and (c),(d) case 2. The white line indicates the initial centerline of the cloud at $z = 16.25$ km.

the fixed heat source, also breaks the symmetry about the horizontal centerline of the cloud. The change in the shape and position of the cloud in case 1 is illustrated in Figs. 8a,b; in both panels the white horizontal line marks the initial centerline of the cloud. The top and bottom of the cloud rise roughly 100 m during the 6-h simulation, whereas the region of highest cloud ice concentration, where the heating and vertical velocities are strongest, rises roughly 200 m.

Qualitatively similar results are obtained in case 2, which differs from case 1 in that the initial cloud is horizontally uniform over a length of 80 km before tapering to zero at its edges and the background static stability is higher above the cloud than below. As shown in Figs. 7b,d,f, the vertical variations in N lead to an even more pronounced departure from symmetry about the $z = 16.25$-km level, and the increase in the width of the region of high ice crystal concentration and strong heating leads to larger potential temperature and horizontal velocity perturbations. The upward vertical velocities in case 2 are slightly weaker, although the downward velocities outside the cloud and the horizontally integrated upward displacements within the cloud are greater than in case 1. As is apparent in Figs. 8c,d, the distortion of the cloud edge (due to horizontal outflow at the top of the cloud and inflow at the bottom) is also more pronounced. In case 2 the bottom of the cloud again ascends about 100 m during the 6-h simulation, but the ascent of both the top and the center of the cloud is slightly less than in case 1.

The fields in these numerical simulations never reach a true steady state because of the continuous changes in

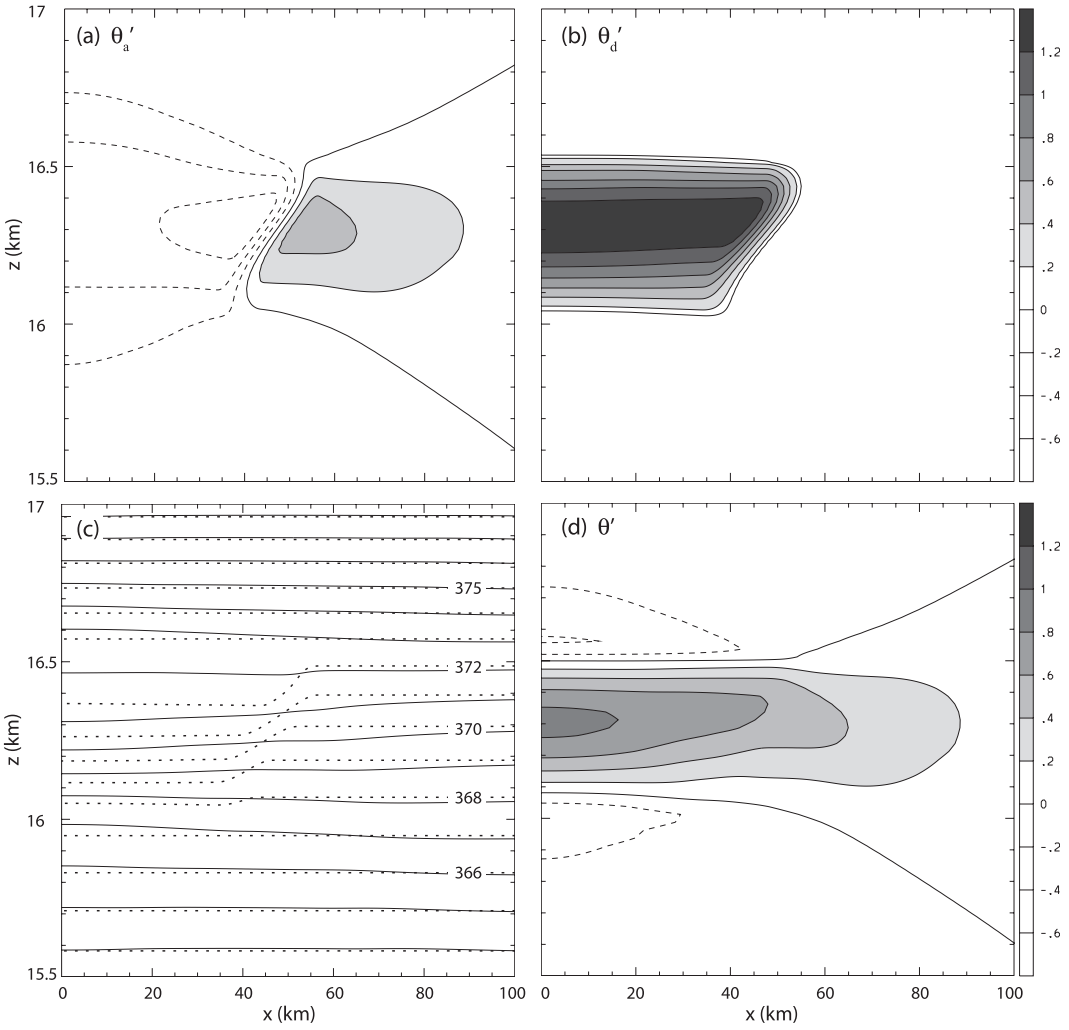

FIG. 9. Potential temperature fields at $t = 6$ h in case 2: (a) θ'_a (b) θ'_d (c) θ (solid) and $\overline{\theta}(z) + \theta'_d$ (dotted), (d) θ'. The contour interval in (a),(b), and (d) is 0.2 K; in (c) it is 1 K. Shaded contours show perturbations greater than 0.2 K.

the cloud geometry. Nevertheless, because the ice particles move slowly, the discussion in section 2b still provides a rough description of the approach of the numerical solutions to steady state. For example, in case 1 the vertical velocity at the center of the cloud is 5.6 mm s^{-1} at $t = 6$ h, which is 82% of the steady-state vertical velocity in the center of the cloud in the case with fixed heating [for which $w_{ss}(0, 0) = Q_0/N^2 = 6.8$ mm s^{-1}]. According to (13) and (15), the time required to reach 82% of $w_{ss}(0, 0)$ in the fixed-heating case is 5.2 h, which is a reasonable estimate of the 6-h time actually required to develop the same w in the numerical simulation.

When assessing the possible role of TTL cirrus in stratospheric–tropospheric exchange, a key question centers on the degree of cross-isentropic transport induced by the radiative heating, and this is illustrated for case 2 in Fig. 9. The potential temperature perturbation may be decomposed as the sum of perturbations due to the adiabatic redistribution of the mean stratification, θ'_a, and a remainder due to diabatic heating, θ'_d. There is no latent heating or cooling in these simulations, and the parameterized subgrid-scale turbulent mixing never becomes active, so θ'_d may also be interpreted as the time integral of Q along each air parcel trajectory.

As shown in Fig. 9a, negative values of θ'_a are produced by rising motion within, above, and below the cloud, whereas subsidence produces positive θ'_a outside the lateral cloud edge. On the other hand, IR heating produces positive values of θ'_d inside the cloud (Fig. 9b), and these more than compensate for the adiabatic cooling, creating a horizontally extensive layer of positive θ' (Fig. 9d). Figure 9c indicates the extent to which the actual potential temperature distribution responds

to the heating. The hypothetical field $\overline{\theta}(z) + \theta'_d$ (dashed lines) shows the potential temperature that would develop if all radiative heating resulted solely in local temperature increases. Not surprisingly, the atmosphere adjusts so that the maximum slope of the isentropes for the actual θ field is much less than that for $\overline{\theta}(z) + \theta'_d$. The energy budget analysis from the linear model (Fig. 4a) suggests that roughly one-third of the total energy input by radiative heating is converted to perturbation kinetic energy.

4. Conclusions

Analytic solutions were obtained to an initial value problem in which a fixed steady heat source representative of the radiative heating in TTL cirrus is turned on instantaneously. These solutions show rising motion in the heated region along with horizontal inflow toward the base of the heat source and horizontal outflow from its top. A layer of heated air gradually extends far beyond the lateral edges of the heat source; this heating is produced by adiabatic subsidence at the leading edge of the expanding disturbance. Thinner layers of air cooled by ascent appear above and below the heat source and propagate laterally away from their region of formation. These disturbances are gravity waves. After the initial transient, they are generated by steady forcing so their frequencies are nearly zero, and therefore they propagate almost horizontally.

According to the functional dependence of the perturbation fields predicted by the analytic solution for the fixed heat source, the vertical velocity depends only on the strength of the heating, but the magnitudes of the horizontal velocity and temperature perturbations are also linearly proportional to the cloud's width. The lateral propagation of the temperature perturbations occurs at gravity wave phase speeds, which, in contrast to the amplitudes of the perturbation fields, are independent of the strength of the heating.

Very similar solutions were obtained using a mesoscale cloud model without true microphysics: ice crystal sedimentation was neglected and, for purposes of the radiative heating calculations, all crystals were assumed to maintain a radius of 4.2 μm. The similarity between the analytic solutions and those computed by the model is particularly close in case 1, in which the background temperature and initial cloud distribution for the numerical simulation are almost identical to those for the analytic solution. Nevertheless, even in case 2, where a more realistic atmospheric structure and a more uniform initial cloud distribution are simulated, the numerical and analytic solutions have the same qualitative character.

The primary difference between the numerical and the analytic solutions comes from the nonlinear advection of the cloud ice field by the perturbation wind field, which slowly lifts the cloud while narrowing its base and widening its top: the cloud tends to self-loft and self-spread because of nonlinear advection. In cases 1 and 2 the maximum heating was 3 K day^{-1}, which produced maximum vertical velocities at $t = 6$ h of 5.6 and 4.5 mm s^{-1}. These updrafts are substantially stronger than the 3.2 mm s^{-1} terminal velocity estimated for an ice crystal with the nominal radius of 4.2 μm (Böhm 1989) used in this simulation, suggesting that radiative heating may indeed maintain some TTL cirrus against sedimentation. Recent observations (Lawson et al. 2008) show that at least some TTL cirrus have considerably larger mean effective radii (8.8 μm) that would fall more rapidly. In fact, there is little intrinsic significance to the nominal 4.2-μm radius chosen for the ice crystals in this study because we do not include any true microphysical processes; the crystal radius and ice water content of the cloud were chosen together to give 3 K day^{-1} of IR heating to match the observations of Comstock et al. (2002) and BHM. We are incorporating a bin microphysics scheme into the model and will explore longer simulations of clouds with nonuniform ice crystal distributions to gain an understanding of the role of sedimentation.

Because our cloud model does not include sedimentation, we cannot definitively determine the ultimate fate of the TTL cirrus present at the initial time of our simulations. Nevertheless, the simulations presented here demonstrate that mesoscale circulations induced by the radiative heating of a cirrus layer that is optically thin in the IR will tend to limit the increase in temperature within the cloud to a value considerably below that which would be achieved if its temperature simply increased at the same rate as the local radiative heating. Two processes are involved. First, the radiative energy absorbed by the ice particles is redistributed horizontally by gravity waves over a much larger region than the cloud itself. Second, the heating produces ascent in the cloudy layer, which tends to cool the air by adiabatic expansion. Any tendency of radiative heating to warm the cloud and dissipate it through sublimation is thereby greatly reduced (cf. the solid and dotted–dashed lines in Fig. 3b).

In addition to the simple treatment of microphysics, there are several other ways in which these simulations do not provide a complete model of the TTL cirrus. We do not account for the initial nucleation of the ice crystals or large-scale motion fields that might be responsible for TTL cirrus formation. Once a cloud is formed, however, radiative heating will tend to force circulations

of the type considered above, and at least to first order, these circulations are likely to be superimposed on any large-scale perturbation. We will explore the influence of larger-scale motions on the clouds in future research and examine the role radiatively heated TTL cirrus may play in the transport of water from the troposphere to the stratosphere.

Acknowledgments. This paper benefited from the comments of two anonymous reviewers. This research has been supported by National Science Foundation (NSF) Division of Atmospheric Sciences Grants ATM-022544 and ATM-0506589 and by the University of Washington Office of Research.

REFERENCES

Ackerman, T. P., K.-N. Liou, F. P. Valero, and L. Pfister, 1988: Heating rates in tropical anvils. *J. Atmos. Sci.,* **45,** 1606–1623.

Blossey, P. N., and D. R. Durran, 2008: Selective monotonicity preservation in scalar advection. *J. Comput. Phys.,* **227,** 5160–5183.

Boehm, M. T., J. Verlinde, and T. P. Ackerman, 1999: On the maintenance of high tropical cirrus. *J. Geophys. Res.,* **104,** 24 423–24 433.

Böhm, H. P., 1989: A general equation for the terminal fall speed of solid hydrometeors. *J. Atmos. Sci.,* **46,** 2419–2427.

Bougeault, P., 1983: A nonreflective upper boundary condition for limited-height hydrostatic models. *Mon. Wea. Rev.,* **111,** 420–429.

Comstock, J. M., T. P. Ackerman, and G. G. Mace, 2002: Ground-based lidar and radar remote sensing of tropical cirrus clouds at Nauru Island: Cloud statistics and radiative impacts. *J. Geophys. Res.,* **107,** 4714, doi:10.1029/2002JD002203.

Corti, T., B. Luo, Q. Fu, H. Vömel, and T. Peter, 2006: The impact of cirrus clouds on tropical troposphere-to-stratosphere transport. *Atmos. Chem. Phys.,* **6,** 2539–2547.

Danielsen, E. F., 1982: A dehydration mechanism for the stratosphere. *Geophys. Res. Lett.,* **9,** 605–608.

Dessler, A. E., S. P. Palm, W. D. Hart, and J. D. Spinhirne, 2006: Tropopause-level thin cirrus coverage revealed by ICESat/Geoscience Laser Altimeter System. *J. Geophys. Res.,* **111,** D08203, doi:10.1029/2005JD006586.

Durran, D. R., 1999: *Numerical Methods for Wave Equations in Geophysical Fluid Dynamics*. Springer-Verlag, 465 pp.

——, and J. B. Klemp, 1983: A compressible model for the simulation of moist mountain waves. *Mon. Wea. Rev.,* **111,** 2341–2361.

Gettelman, A., P. M. de F. Forster, M. Fujiwara, Q. Fu, H. Vomel, L. K. Gohar, C. Johanson, and M. Ammerman, 2004: Radiation balance of the tropical tropopause layer. *J. Geophys. Res.,* **109,** D07103, doi:10.1029/2003JD004190.

Gill, A. E., 1982: *Atmosphere—Ocean Dynamics*. Academic Press, 662 pp.

Jensen, E. J., O. B. Toon, L. Pfister, and H. B. Selkirk, 1996a: Dehydration of the upper troposphere and lower stratosphere by subvisible cirrus clouds near the tropical tropopause. *Geophys. Res. Lett.,* **23,** 825–828.

——, ——, H. B. Selkirk, J. D. Spinhirne, and M. R. Schoeberl, 1996b: On the formation and persistence of subvisible cirrus clouds near the tropical tropopause. *J. Geophys. Res.,* **101,** 21 361–21 375.

Kato, S., T. P. Ackerman, J. H. Mather, and E. E. Clothiaux, 1999: The *k*-distribution method and correlated-*k* approximation for a shortwave radiative transfer model. *J. Quant. Spectrosc. Radiat. Transfer,* **62,** 109–121.

Klemp, J. B., and D. Durran, 1983: An upper boundary condition permitting internal gravity wave radiation in numerical mesoscale models. *Mon. Wea. Rev.,* **111,** 430–444.

Lawson, R., B. Pilson, B. Baker, Q. Mo, E. Jensen, L. Pfister, and P. Bui, 2008: Aircraft measurements of microphysical properties of subvisible cirrus in the tropical tropopause layer. *Atmos. Chem. Phys.,* **8,** 1609–1620.

Lilly, D. K., 1988: Cirrus outflow dynamics. *J. Atmos. Sci.,* **45,** 1594–1605.

Lin, Y. L., and R. B. Smith, 1986: Transient dynamics of airflow near a local heat source. *J. Atmos. Sci.,* **43,** 40–49.

Liu, C., 2007: Geographical and seasonal distribution of tropical tropopause thin clouds and their relation to deep convection and water vapor viewed from satellite measurements. *J. Geophys. Res.,* **112,** D09205, doi:10.1029/2006JD007479.

Mace, G. G., Q. Zhang, M. Vaughan, R. Marchand, G. Stephens, C. Trepte, and D. Winker, 2009: A description of hydrometeor layer occurrence statistics derived from the first year of merged Cloudsat and CALIPSO data. *J. Geophys. Res.,* **114,** D00A26, doi:10.1029/2007JD009755.

McFarquhar, G. M., A. J. Heymsfield, J. Spinhirne, and B. Hart, 2000: Thin and subvisual tropopause tropical cirrus: Observations and radiative impacts. *J. Atmos. Sci.,* **57,** 1841–1853.

Nicholls, M. E., R. A. Pielke, and W. R. Cotton, 1991: Thermally forced gravity waves in an atmosphere at rest. *J. Atmos. Sci.,* **48,** 1869–1884.

Pandya, R., D. Durran, and C. Bretherton, 1993: Comments on ''Thermally forced gravity waves in an atmosphere at rest.'' *J. Atmos. Sci.,* **50,** 4097–4101.

Peter, T., and Coauthors, 2003: Ultrathin tropical tropopause clouds (UTTCs): I. Cloud morphology and occurrence. *Atmos. Chem. Phys.,* **3,** 1083–1091.

Pfister, L., and Coauthors, 2001: Aircraft observations of thin cirrus clouds near the tropical tropopause. *J. Geophys. Res.,* **106,** 9765–9786.

Toon, O. B., C. P. Mckay, T. P. Ackerman, and K. Santhanam, 1989: Rapid calculation of radiative heating rates and photodissociation rates in inhomogeneous multiple scattering atmospheres. *J. Geophys. Res.,* **94,** 16 287–16 301.

Wang, P.-H., P. Minnis, M. P. McCormick, G. S. Kent, and K. M. Skeens, 1996: A 6-year climatology of cloud occurrence frequency from Stratospheric Aerosol and Gas Experiment II observations (1985–1990). *J. Geophys. Res.,* **101,** 29 407–29 429.

Winker, D. M., and C. R. Trepte, 1998: Laminar cirrus observed near the tropical tropopause by LITE. *Geophys. Res. Lett.,* **25,** 3351–3354.